Ultrafast charge transfer in anisotropic black phosphorus/TiS₃ heterostructures for photoconversion

Lili Zhang [1,*], Qiuyu Wang,[1] Leyao Wang,[1] Liyuan Wang,[1] Jin Zhao [2,3,4,†] and Shunfang Li [1,5,‡]

[1]*Key Laboratory of Material Physics, Ministry of Education, School of Physics and Microelectronics,*
Zhengzhou University, Zhengzhou 450001, China
[2]*Department of Physics and ICQD/Hefei National Research Center for Physical Sciences at the Microscale,*
University of Science and Technology of China, Hefei 230026, China
[3]*Department of Physics and Astronomy and the IQ Initiative, University of Pittsburgh, Pittsburgh, Pennsylvania 15260, USA*
[4]*Hefei National Laboratory, University of Science and Technology of China, Hefei 230088, China*
[5]*Institute of Quantum Materials and Physics, Henan Academy of Sciences, Zhengzhou 450046, China*

Construction of two-dimensional van der Waals (vdW) heterostructure has been well recognized to provide an avenue towards designing functional optoelectronic and photovoltaic devices. Here, a type-II vdW heterostructure consisting of anisotropic black phosphorus (BP) and TiS₃ possessing ultrafast interlayer charge transfer for photoconversion is established using *ab initio* nonadiabatic molecular dynamics with HSE06 hybrid functional. The present results demonstrate that the ultrafast interlayer electron and hole transfer occur within 42 and 467 fs, respectively, which is mainly ascribed to the electron-phonon coupling dominantly contributed by an interlayer breathing mode and the stretching mode of TiS₃ induced by in-plane vibration of interfacial S-S pairs. Moreover, it is discovered that the interlayer charge transfer process can be effectively controlled by the external electric field (EEF); i.e., positive (negative) EEF can sustain (slow down) the ultrafast carrier dynamics and facilitate (degenerate) the separation of electron and hole. The present findings pave the way to developing high-performance functional optoelectronic devices based on two-dimensional vdW heterostructure.

I. INTRODUCTION

Two-dimensional (2D) atomic-layer materials have emerged as promising platforms for high-performance optoelectronic and photovoltaic applications due to their unique optical, electronic, and mechanical properties [1–4]. Based on the weak interlayer van der Waals (vdW) interaction and intralayer strong covalent bonding, one can establish functional heterostructures via stacking various 2D materials vertically without the constraint of lattice mismatch, which provides more opportunities for exploring new physics and practical applications [5–10]. Moreover, the design of a potential vdW heterostructure with type-II band alignment is expected to effectively separate the photoexcited carrier into consisting components and reduce the undesirable electron-hole recombination [11–15].

Particularly, 2D anisotropic materials with moderate band gap and reasonably high carrier mobility demonstrate great potential for next-generation electronic devices such as field-effect transistors and polarization-sensitive photodetectors [16–20]. Black phosphorus (BP) as a representative of such anisotropic material is recognized with its tunable thickness-dependent direct band gap ranging 1.5–2.0 eV for monolayer to 0.3 eV for bulk, high hole mobility up to $1000\,\mathrm{cm^2/V\,s}$ and superior mechanical flexibility [21–25]. However, BP is easy to oxidize in ambient conditions, thus various effective encapsulation and passivation methods have been adopted to protect BP from air contact [26,27]. Titanium trisulfide (TiS₃) is an emerging member of the transition metal trichalcogenides family possessing not only dynamical and thermal stabilities but also promising electronic properties such as a direct band gap of ∼1.0 eV and high anisotropic electron mobility up to $10\,000\,\mathrm{cm^2/V\,s}$ [28–30]. Apart from the in-plane electronic anisotropy, it also exhibits ultrahigh efficiency of the visible photoresponse [31]. Thus, it is proposed that the combination of BP and TiS₃ with both high hole and electron mobility can collectively provide great potential applications in optoelectronics and photovoltaics. Specifically, the TiS₃ protecting overlayer can not only suppress the oxidation of BP in air conditions, but also lead to greatly improved functionalities due to the separation of photogenerated carriers across the heterostructure interface.

The performance of heterostructure in light harvesting and photoconversion is dominated by the dynamics of photogenerated charge carriers that are mostly determined by band alignment and interlayer coupling, which in turn inspires researchers to explore various approaches to modulate the interlayer coupling and electronic properties to improve the performances of heterostructures for practical application. Wu *et al.* summarized different performance modulation techniques including mechanical based, external fields assisted, and particle beam irradiation based methods to tune the interlayer coupling and properties in vdW heterostructure [32]. Among the above methods, external electric field (EEF) as a nondestructive and reversible strategy is recognized as

*Corresponding author: zhlili@zzu.edu.cn
†Corresponding author: zhaojin@ustc.edu.cn
‡Corresponding author: sflizzu@zzu.edu.cn

one of the most efficient ways to manipulate the electric and optical properties of vdW heterostructures [33,34]. The previous studies of electric field mostly focused on its effects on the electronic and optical properties, phase transition, valley spintronics [35–41]. For example, Wang *et al.* studied the effect of external electric field on modulation the band alignment, optical properties, and further energy conversion efficiency [40]. Cheng *et al.* reported the emergence of electric-field-tunable interfacial ferromagnetism in 2D antiferromagnet heterostructure [41]. Recently, Liu *et al.* investigated the ultrafast interlayer charge transfer in graphene/WS$_2$ heterostructure tunable by the electric field which changes the coupling between donor and acceptor states and hence the charge transfer rate [33]. However, the introduced influence by electric field is not only the band alignment and corresponding coupling between donor and acceptor states, but also the vibration phonon modes and charge carrier relaxation pathways. Thus, it is significant to comprehensively understand the underlying mechanism of electric field modulation on interfacial charge transfer dynamics, which essentially determines the overall performance of functional devices.

Here, using *ab initio* nonadiabatic molecular dynamics (NAMD) simulation, we design a 2D vdW heterostructure as BP/TiS$_3$ and then investigate the ultrafast interfacial charge transfer process and its modulation by EEF. Our results demonstrate that photoexcited electron and hole transfer at the interface of BP/TiS$_3$ heterostructure with type-II band alignment take within 42 and 467 fs, respectively. Further analysis shows that the ultrafast electron and hole transfer of BP/TiS$_3$ heterostructure is dominantly governed by the electron-phonon (*e-ph*) coupling contributed by low frequency interlayer breathing mode at 46 cm^{-1} induced by vdW interaction and high frequency A_g^{S-S} mode of TiS$_3$ around 600 cm^{-1} induced by in-plane vibration of the interfacial S-S pairs. Moreover, the interlayer charge transfer presents strong dependence on EEF; i.e., negative EEF slows down the carrier dynamics whereas positive EEF can sustain the ultrafast carrier dynamics and facilitate the separation of electron and hole. The present results provide a valuable option in design and modulation of high-performance 2D functional optoelectronic devices and photocatalysts.

II. COMPUTATIONAL METHODS

The *ab initio* NAMD calculations are performed using HEFEI-NAMD code with phase correction version [42,43], which augments the Vienna *ab initio* Simulation Package (VASP) with the NAMD capabilities within time-dependent Kohn-Sham theory and surface hopping method based on classical path approximation similar to Refs. [44,45]. This NAMD approach is computationally tractable and has been utilized in several studies of photoexcited carrier dynamics in various materials [14,46–50]. The projector-augmented wave (PAW) method and the Perdew-Burke-Ernzerhof (PBE) functional under the generalized gradient approximation (GGA) are used to optimize the structure [51,52]. Then the hybrid Heyd-Scuseria-Ernzerhof (HSE06) functional is adopted to get accurate electronic structure. The kinetic energy cutoff for plane-wave expansion is set to be 450 eV. All the structures are fully relaxed until the total energy and atomic forces are

smaller than 10^{-5} eV and 0.01 eV/Å, respectively. A vacuum space of 16 Å in the z direction is used to eliminate spurious interaction between the periodic images of the 2D materials. The vdW interactions are described with Grimme's DFT-D3 approach [53]. The Brillouin zone is sampled only at the Γ point for the 2 × 4 TiS$_3$ supercell matching with the 3 × 3 BP with negligible lattice mismatch as discussed later. After the geometry optimization, the systems are heated to 300 K by repeated velocity rescaling. Then, a 5-ps *ab initio* molecular dynamics trajectory is obtained in the microcanonical ensemble with 1 fs atomic time step. The NAMD simulation results are based on averaging over 100 random initial configurations and 20 000 surface-hopping trajectories sampled for each initial structure. For the frozen phonon method, atomic trajectories are generated along a selected phonon mode. The average kinetic energy of each phonon mode is determined by $\langle K \rangle = 3N \frac{1}{2} K_B T$, where N is the number of atoms. In this work, we use $T = 300$ K to generate a reasonable vibrational amplitude. More details of the NAMD theory can be found in the Supplemental Material [54] (see also Refs. [55–58] therein). It is worth mentioning that the HSE06 hybrid functional is adopted to give accurate electronic properties in our NAMD simulation with an expensive calculation cost. The decoherence effect is not considered in our calculation. Usually, when we study the charge carrier dynamics such as electron-hole recombination dynamics, which has a very long time scale (usually nanosecond), the decoherence needs to be considered, because these processes take much longer time than the decoherence time scale and then the coherent electron states tend to collapse to a pure state.

III. RESULTS AND DISCUSSION

As a starting point, we first introduce the geometric configuration and electronic properties of BP/TiS$_3$ heterostructure, as shown in Fig. 1(a). The optimized lattice constants of TiS$_3$ (BP) along the a and b directions are 4.98 (3.30) and 3.39 (4.57) Å, respectively, which are in good agreement with previous reports [22,23,28,30]. Then, we construct the BP/TiS$_3$ vdW heterostructure using the lattice parameter of 2 × 4 TiS$_3$ supercell to cover over a 3 × 3 cell of BP, which minimizes the lattice mismatch to 0.6% and 1.04% along a and b directions, respectively. The optimized atomic positions of heterostructure are presented in the Supplemental Material [54]. The calculated band gap of the BP/TiS$_3$ vdW heterostructure is 0.68 eV, which is smaller than that of monolayer TiS$_3$ (1.14 eV) and BP (1.59 eV), respectively. The binding energy per P atom between BP and TiS$_3$ is calculated according to the formula $E_b = (E_{BP/TiS_3} - E_{BP} - E_{TiS_3})/N_P$, where E_{BP/TiS_3}, E_{BP}, and E_{TiS_3} are the total energies of BP/TiS$_3$ heterostructure, monolayer BP, and TiS$_3$, respectively, and N_P is the number of P atoms in the unit cell. The average binding energy per P atom is calculated to be -79.78 meV, which is comparable with that of other heterostructures [59,60]. The negative binding energy indicates that the heterostructure is thermodynamically favorable, and the lower the E_b is, the stronger interlayer interaction between BP and TiS$_3$ is. This is further verified by the differential charge density as shown in Fig. S1(a) in the Supplemental Material; a notable charge redistribution occurs at the interface of BP/TiS$_3$
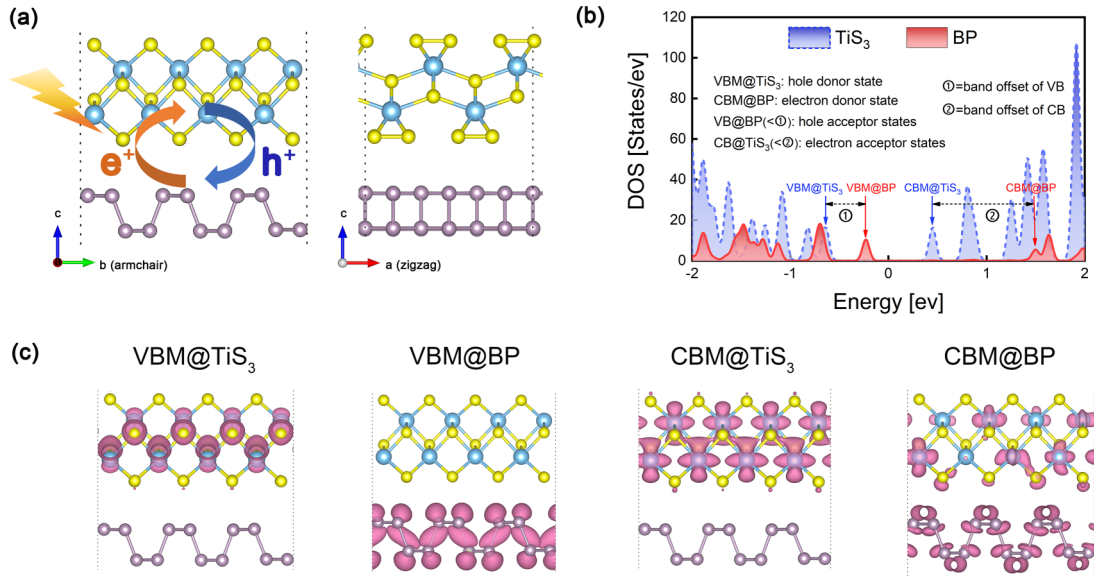
FIG. 1. (a) Optimized geometry and (b) DOS of BP/TiS$_3$ vdW heterostructure with purple, light blue, and yellow balls representing P, Ti, and S atoms, respectively. Schematic diagram of photoexcited carrier dynamics is presented in (a). (c) Charge density distributions for VBM@TiS$_3$, VBM@BP, CBM@TiS$_3$, and CBM@BP with an isosurface value of 0.0006 e/bohr^3.

heterostructure. From the projected density of states (PDOS) shown in Fig. 1(b), the valence band maximum (VBM) and the conduction band minimum (CBM) of BP/TiS$_3$ system are respectively contributed by BP and TiS$_3$, indicating that this heterostructure possesses a type-II band alignment, which is beneficial for effective separation of photoexcited electrons and holes. The band offsets in the VB and CB parts are 0.41 and 1.05 eV, respectively. Figure 1(c) demonstrates the charge densities of the key energy states involved in the photogenerated charge transfer process. It can be seen that the electron donor state is hybridized by BP and TiS$_3$, whereas the hole donor and acceptor states are respectively contributed by TiS$_3$ and BP. Moreover, the photoabsorption spectra present anisotropy with high photoresponse along the armchair direction; see Fig. S1(b) in the Supplemental Material.

Now, we turn to the dynamic processes of charge transfer by photoexcitation. As implied in Fig. 1(b), given that the photoexcitation initially generates intralayer electrons and holes in BP and TiS$_3$, respectively, then the electrons at CBM@BP transfer to CB@TiS$_3$, and the residing holes at VBM@TiS$_3$ transfer to VB@BP. Figure 2 presents the dynamics of photoinduced charge transfer and corresponding energy relaxation in BP/TiS$_3$ heterostructure. As seen in Figs. 2(a) and 2(b), the ultrafast electron transfer from CBM@BP to CB@TiS$_3$ takes within 42 fs, which is obtained by exponential fitting using $f(t) = \exp(-t/\tau)$. The hole transfer from VBM@TiS$_3$ to VB@BP occurs within 467 fs. The fast charge carrier dynamics can be further confirmed by the time-dependent average energy evolution of the involved energy states as deduced by evaluating the electron and hole probability distributions of the states from the NAMD. As shown in Figs. 2(c) and 2(d), the average electron (hole) energy loss 1.0 (0.2) eV from initial 1.6 (-0.8) eV to 0.6 (-0.6) eV within 1 ps during the charge transfer dynamic process. The underlying reason for ultrafast charge transfer can be rationalized by strong interlayer coupling, as discussed shortly.

We now investigate the role of EEF in modulation of the photoexcited charge transfer at the interface of BP/TiS$_3$ heterostructure. First, we analyze the electronic properties of this heterostructure with EEF ranging -0.3 to $+0.3$ V/Å. Here, the positive z direction of the lattice cell is referred to as the positive direction of EEF. As shown in Fig. 3(a), the applied EEF has a negligible influence on the electronic states of BP, however it effectively shifts the energy states of TiS$_3$ [61]. Such contrasting behaviors can be rationalized by the Ti-S ionic binding in TiS$_3$ which is more sensitive to EEF, as compared to the P-P covalent binding in BP. Specifically, when the EEF is negative (positive), the electronic states of TiS$_3$ undergo an upward (downward) shift. This shift has two
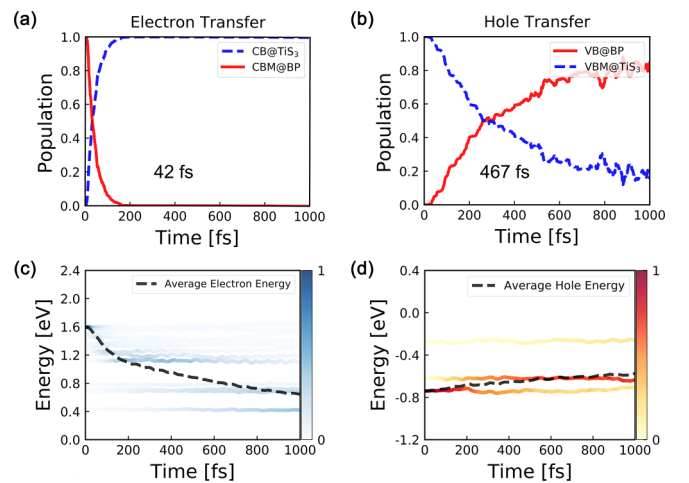

FIG. 2. Time-dependent populations (a),(b) and energy evolutions (c),(d) of electron and hole in BP/TiS$_3$ heterostructure. Panels (a) and (c) are for electron, (b) and (d) are for hole. The black dashed lines in (c) and (d) represent the time-dependent average energies of the involved electronic states.
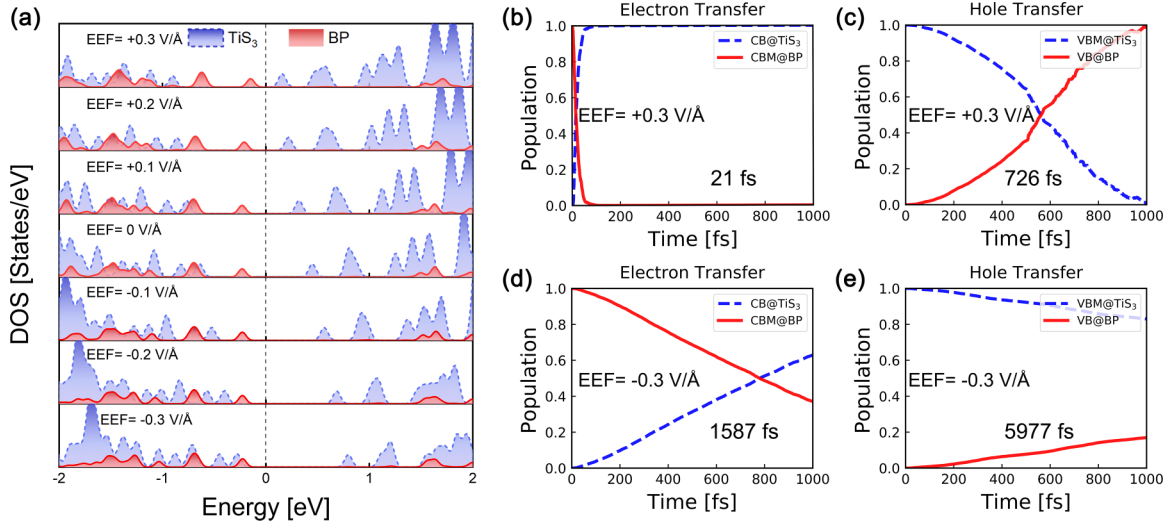
FIG. 3. (a) DOS of BP/TiS$_3$ heterostructure under EEF with the strength ranging -0.3 to $+0.3$ V/Å. (b)–(e) Time-dependent electron and hole population during the charge transfer dynamics at the interface of BP/TiS$_3$ heterostructure under the EEF of $+0.3$ V/Å (b),(c) and -0.3 V/Å (c),(d).

primary consequences. First, it results in a decrease (increase) in the band offset of both VB and CB. Second, it leads to a reduction (increase) in the density of both electron and hole acceptor states. Moreover, the EEF-dependent electronic structure can also be verified by charge density distributions of the key energy states involved in charge transfer dynamics; see Fig. S2 in the Supplemental Material [54].

Next, taking $+0.3$ and -0.3 V/Å as two typical values of the EEF, we comparatively investigate the role of EEF in modulation of the charge transfer dynamics. Under the EEF of $+0.3$ (-0.3) V/Å, the band offsets in VB and CB parts are 0.75 (0.05) and 1.38 (0.77) eV, respectively, which are larger (smaller) than that of BP/TiS$_3$ heterostructure without EEF. Figures 3(b) and 3(c) present the photoexcited carrier dynamics under the EEF of $+0.3$ V/Å. The electron and hole transfer processes still maintain at ultrafast time scale with 21 and 726 fs, respectively. In contrast, when EEF $= -0.3$ V/Å, the charge transfer dynamics is suppressed significantly with time scales of 1587 and 5977 fs; see Figs. 3(d) and 3(e). Thus, one can see that the interlayer charge transfer processes can be effectively modulated by EEF, which provides convenient application in optoelectronics.

To understand the charge transfer dynamics across the interface and its response to EEF, we analyzed the nonadiabatic coupling (NAC) which determines the time scale of electron and hole transfer. In the *ab initio* NAMD simulation, the NAC can be written as

$$d_{jk} = \langle \varphi_j | \frac{\partial}{\partial t} | \varphi_k \rangle = \frac{\langle \varphi_j | \nabla_R H | \varphi_k \rangle}{\varepsilon_k - \varepsilon_j} \dot{R},$$

where H is the Kohn-Sham Hamiltonian, with φ_j, φ_k, ε_j, and ε_k corresponding to the wave functions and eigenvalues of the electronic states j and k, and $\dot{R}$ representing the velocity of the nuclei, respectively. Thus, NAC is determined by three terms: *e-ph* coupling element $\langle \varphi_j | \nabla_R H | \varphi_k \rangle$, energy gap $\varepsilon_k - \varepsilon_j$, and nuclear velocity $\dot{R}$. Clearly, a relatively large NAC corresponding to the fast charge transfer process is facilitated by strong *e-ph* coupling and a small energy gap. NAC determines

the coupling between two electronic states Ψ_i and Ψ_j. Generally, the larger NAC is, the shorter time scale is, and the faster charge transfer dynamics is. However, during the charge transfer dynamics, it may involve more than one electronic state. For example, starting from Ψ_i, the electron can transfer to Ψ_j or Ψ_k. Namely, in this case there are two charge transfer pathways $\Psi_i \rightarrow \Psi_j$ and $\Psi_i \rightarrow \Psi_k$, while NAC$_{i,j}$ and NAC$_{i,k}$ determine the transfer probability of these two pathways. The number of charge transfer pathways is determined by the DOS. Therefore, one can see that the DOS does not directly enter the NAC equation, however, it also affects the charge transfer dynamics. As shown in Fig. 4 and Table I, there are 1, 2, 3 electronic states as hole acceptor states for the case of EEF $= -0.3$, 0, $+0.3$ V/Å, respectively, which can provide 1, 2, 4 charge transfer pathways. Although the NAC of EEF $= -0.3$ V/Å is as large as 14.05 meV, which is larger than 6.39 meV (path I for EEF $= 0$ V/Å) and 1.75 meV (path I for EEF $= +0.3$ V/Å). However, it has only one charge transfer pathway, so that it needs a longer time to accept the hole. For the case of EEF $= 0$, $+0.3$ V/Å, there are two and four pathways to accept the hole, respectively. Thus, the hole transfer dynamics under EEF $= -0.3$ V/Å (with 5977 fs) is slower than that of EEF $= 0$, $+0.3$ V/Å. Hence, the charge transfer dynamics is complex which is determined by the relaxation pathways together with NAC.

The reason for electron transfer dynamics faster than hole transfer is mainly ascribed to two aspects. One is the strong coupling between electron acceptors and donor, with the charge density of electron donor distributed on both BP and TiS$_3$, as shown in Fig. 1(c). Contrastingly, the coupling between hole donor and acceptors is small, because their charge distributions are contributed respectively by TiS$_3$ and BP. The other one is that more electron acceptors (CB@TiS$_3$) introduce more charge transfer pathways to accept the photoexcited electron from CBM@BP, as confirmed in Fig. 1(b). Thus, the electron transfer dynamics is faster than hole transfer. Moreover, Table II provides the averaged NAC, band offset, and electron transfer time scale of BP/TiS$_3$
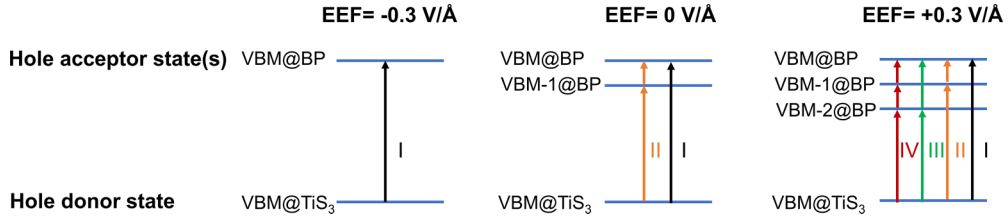
FIG. 4. The schematic hole relaxation pathways of BP/TiS$_3$ heterostructure under EEF of −0.3, 0, +0.3 V/Å.

heterostructure under different values of EEF. One can see that the band offset gets larger linearly along with the EEF strength varying from −0.3, through 0, to +0.3 V/Å, whereas the NAC does not vary with the inverse trend. Thus, the *e-ph* coupling play an essential role in the ultrafast carrier dynamics.

Here we analyze the *e-ph* coupling via the energy evolution of time-dependent Kohn-Sham energy states and their Fourier transform (FT) spectra, see Fig. 5. Essentially, the energy fluctuation amplitude reflects the strength of *e-ph* coupling, and the major phonon frequencies contributed to the above energy fluctuation can be figured out by FT spectra. As shown in Figs. 5(a)–5(c), the fluctuation amplitude of the electronic states under different values of EEF are all around 0.1 eV, and strong hybridization occurs for CBM@BP, i.e., the electron donor state. The EEF has negligible influence on the strength of *e-ph* coupling, however, it introduces a significant effect on the phonon excitation involved in the ultrafast charge transfer processes. First, we consider the case without EEF; see Fig. 5(e). For the electron transfer process, both the electron donor and acceptor states are mainly coupled with the A_g^{S-S} mode at 600 cm^{-1} with a very high peak, which is contributed by S-S pairs interfaced with BP. For the hole transfer process, besides the A_g^{S-S} mode coupled with a hole donor state, low frequency phonon modes below 200 cm^{-1} and other optical phonon modes of BP and TiS$_3$ around 400 cm^{-1} also participate in the *e-ph* coupling, which leads to the fast hole transfer process. Particularly, the A_g^{S-S} phonon mode plays an essential role in both electron and hole transfer dynamics across the interface of BP/TiS$_3$ heterostructure.

Then, we analyze the phonon excitation under EEF. Specifically, when EEF = +0.3 V/Å [see Fig. 5(f)], low frequency phonon modes below 200 cm^{-1} and the optical A_g^{S-S} phonon mode at 600 cm^{-1} mainly contribute to the fast electron and hole transfer dynamics. For the case of EEF = −0.3 V/Å [see

Fig. 5(d)], only low frequency phonon modes below 200 cm^{-1} and optical phonon modes around 400 cm^{-1} participate in the *e-ph* coupling during the charge transfer processes, however, the dominant A_g^{S-S} phonon mode induced by the in-plane vibration of the interfacial S-S pairs is strongly suppressed. Thus, it can be inferred that the charge transfer dynamics of BP/TiS$_3$ heterostructure and its modulation by EEF is primarily determined by the *e-ph* coupling contributed by optical A_g^{S-S} phonon mode and low frequency phonon modes. Especially, once the A_g^{S-S} mode is suppressed, the charge transfer is slowed down.

To further confirm the important role of phonon excitation in the interfacial charge transfer dynamics, taking BP/TiS$_3$ heterostructure without EEF as a prototypical example, we perform the frozen phonon NAMD simulations for low frequency and representative optical phonon modes. Here, we put an emphasis on the excitations of the A_g^{S-S} mode at 600 cm^{-1} and the interlayer breathing mode at 46 cm^{-1} which simultaneously contribute to both electron and hole charge transfer dynamics. The detailed atomic vibrational motions of these two phonon modes are presented in Figs. 6(a) and 6(b). Figures 6(c)–6(f) show the time-dependent electron and hole populations when these two phonon modes are respectively excited, which offers the same trend with that of the BP/TiS$_3$ system shown in Figs. 2(a) and 2(b) when the complex multiple phonon modes are involved. The corresponding time-dependent energy level evolutions along with the phonon excitation are shown in Figs. 6(g) and 6(h). One can see that, for the A_g^{S-S} mode excitation [Fig. 6(g)], the energy states in the CB part vibrate violently with an amplitude of 0.5 eV, representing strong *e-ph* coupling. For the interlayer breathing mode excitation [Fig. 6(h)], a stronger vibration occurs for the energy states in CB (VB) part with larger amplitude of around 1.0 eV (0.5 eV). Such violent fluctuation leads to significant crossing and hybridization between the electronic states of BP

TABLE I. Hole transfer time scale (fs) and the clarification of hole transfer pathways (schematically shown in Fig. 4) with corresponding NAC (meV) and band gap (eV) of BP/TiS$_3$ heterostructure at different values of EEF (V/Å).

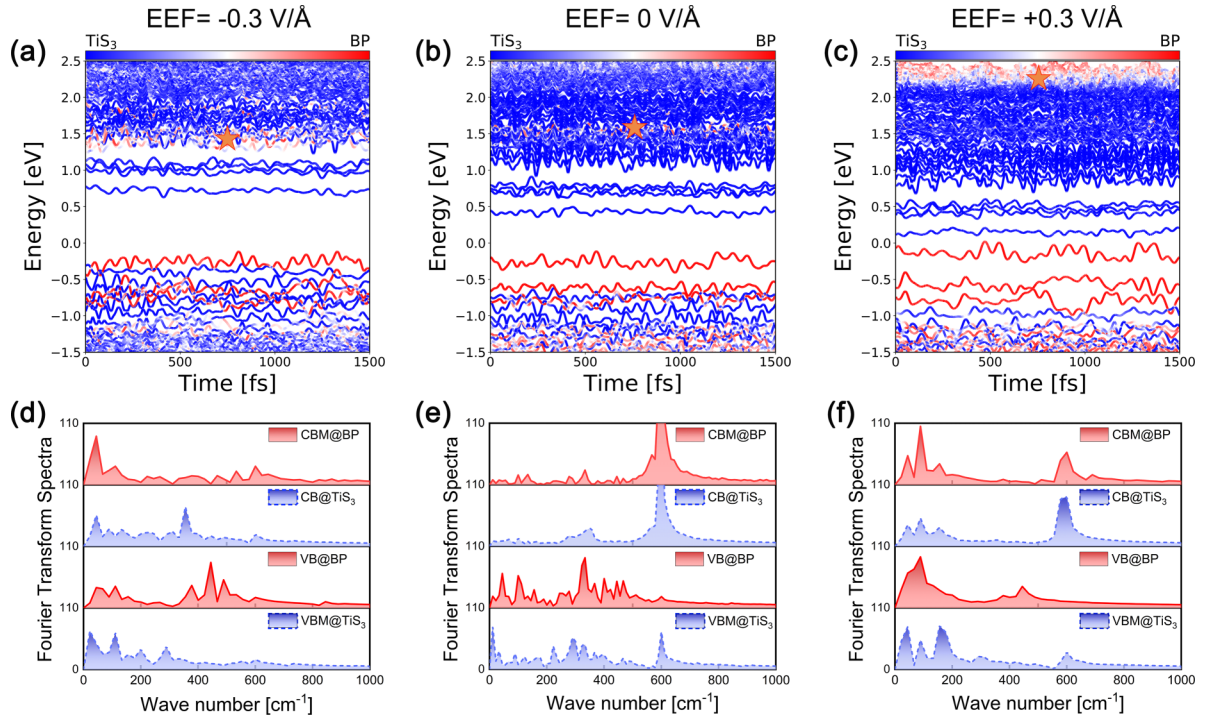| EEF	Time scale		Path I	Path II		Path III			Path IV	
							Hole transfer			
+0.3	726	NAC	1.75	3.25	10.10	16.38	5.74	16.38	13.96	10.10
		band gap	0.82	0.40	0.42	0.17	0.65	0.17	0.23	0.42
0.0	467	NAC	6.39	29.47	13.61					
		band gap	0.45	0.08	0.37					
−0.3	5977	NAC	14.05							
		band gap	0.41							

FIG. 5. Time evolutions of the Kohn-Sham energy levels (a)–(c) and their Fourier transform spectra (d)–(f) for BP/TiS$_3$ heterostructure under the EEF of (a),(d) -0.3 V/Å, (b),(e) 0 V/Å, (c), (f) $+0.3$ V/Å. The stars shown in (a)–(c) represent the initial energy position of photoexcited electron.

and TiS$_3$. We present the charge wave functions of the electron donor state at representative snapshots of MD trajectory under the phonon excitations of 600 and 46 cm^{-1}, as shown in Fig. S3 [54]. It can be seen that the electron wave function is a hybridized distribution at the BP and TiS$_3$, which results in the stronger interlayer coupling and then ultrafast electron transfer. Moreover, we also examined the excitation of other representative optical phonon modes of BP and TiS$_3$ ranging

300–500 cm^{-1}, which also participate in the fast interfacial charge transfer dynamics, as detailed in Figs. S4 and S5 in the Supplemental Material [54].

To the end, we discuss the impact of EEF to interfacial charge transfer dynamics of BP/TiS$_3$ heterostructure. First, the most intuitive cognition is that it shifts the energy positions of electronic states, especially when the EEF is imposed on the ionic component, which results in the variation of band offset
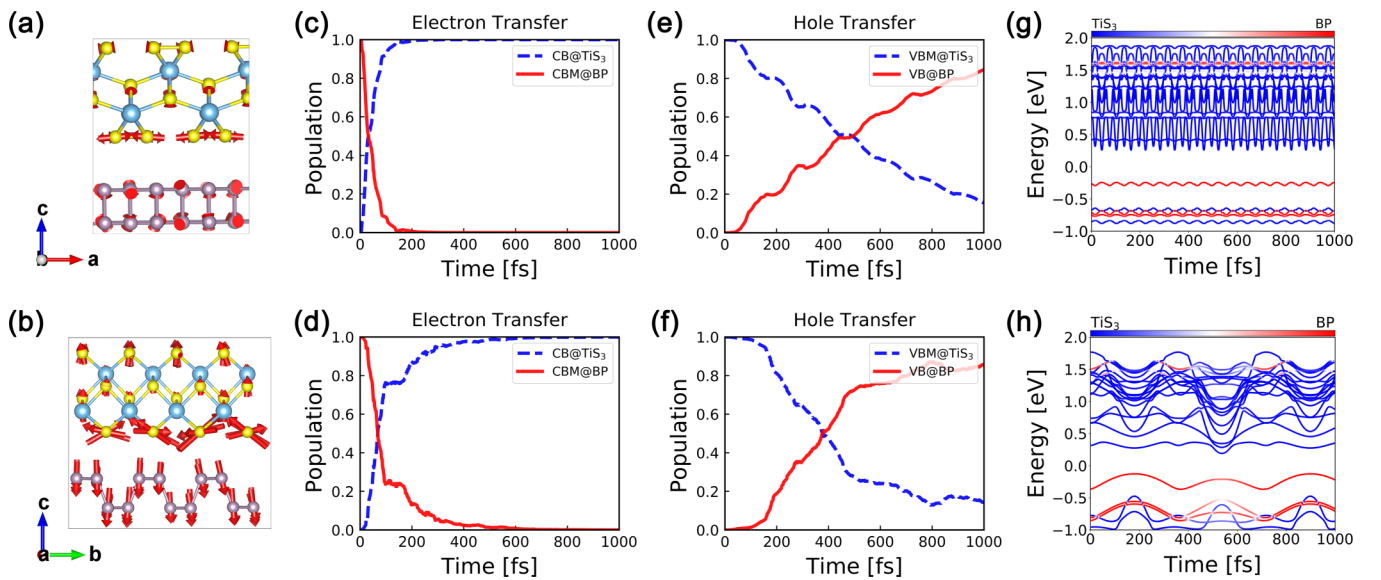

FIG. 6. Atomic vibrational motions of (a) A_g^{S-S} mode at 600 cm^{-1} and (b) interlayer breathing mode at 46 cm^{-1}. (c)–(f) Frozen phonon NAMD simulations of electron and hole transfer in BP/TiS$_3$ system when these two phonon modes are excited, respectively. (g),(h) Time-dependent energy level evolution along with the typical phonon excitation.

TABLE II. Electron transfer time scale (fs), averaged NAC (meV), and band offset (eV) of BP/TiS$_3$ heterostructure at different values of EEF (V/Å).

EEF	Electron transfer		
	Time scale	NAC	Band offset
+0.3	21	20.25	1.38
0.0	42	15.99	1.05
−0.3	1587	7.55	0.77

between charge carrier donor and acceptor states. With the EEF strength varying from −0.3 to +0.3 V/Å, the band offsets at the VB and CB parts increase linearly. However, the time scale of electron and hole transfer dynamics does not vary with the inverse trend. Second, it is noteworthy that it changes the density of electron or hole acceptor states, which results in a profound influence on the charge transfer dynamics. For the hole transfer with EEF = −0.3 V/Å, the hole acceptor states contain only one energy state, and such a "narrow" channel slows down the hole transfer dynamics. Third, the most significant effect is that it modifies the strength of the dominant phonon excitation and corresponding *e-ph* coupling which determines the interfacial charge transfer dynamics. Typically, when EEF = −0.3 V/Å, the dominant stretching $A_\mathrm{g}^\mathrm{S-S}$ mode induced by in-plane vibration of interfacial S-S pairs is strongly suppressed, which also suppresses the hole transfer process. Collectively, the ratio between the hole and electron time scales under negative EEF = −0.3 V/Å is reduced to 3.77, as compared with the value of 11.12 in the case without EEF, as deduced from Table I. However, the positive EEF = +0.3 V/Å results in an enhanced ratio of 34.57, which further facilitates the separation of electron and hole carriers.

The charge transfer at the interface of a 2D vdW heterostructure with ultrafast time scales less than 100 fs has been commonly observed and reported in experiments [62–65]. In this paper, we focus on the relaxation dynamics of charge carriers after photoexcitation. The photoexcitation is not included in the NAMD simulation currently. The photoexcitation process can be simulated by real-time TDDFT (rt-TDDFT). As shown by He and by Zhou *et al.* [66,67], using a laser plus with a photon energy of 1.63 eV, a full width at half maximum (FWHM) of 6.04 fs, and a fluence rate of 13.95 mJ/cm^2 can excite the electron to the excited state within 20 fs. They used rt-TDDFT to generate the initial excited state and then

performed a NAMD simulation to study the carrier relaxation. Due to the very fast time scale (∼21 fs under EEF = +0.3 V/Å), comparable to the duration of standard ultrafast femtosecond laser pulses, there might be interplay between the excitation process and the ultrafast relaxation. The excitation efficiency may be influenced by the ultrafast relaxation, which will be an interesting project to explore in future work.

IV. CONCLUSION

In conclusion, we design a 2D vdW heterostructure of BP/TiS$_3$ with type-II band alignment and demonstrate that the ultrafast interfacial electron and hole transfer dynamics occur within 42 and 467 fs, respectively. The analysis confirms that the ultrafast charge transfer is dominated by two phonon modes: one is an optical $A_\mathrm{g}^\mathrm{S-S}$ phonon mode at 600 cm^{-1} induced by the in-plane vibrations of the interfacial S-S pairs, and the other one is the interlayer breathing mode at 46 cm^{-1} induced by the interfacial vdW interaction. The excitation of these two phonon modes enhances the interlayer coupling, which results in ultrafast charge carrier transfer dynamics. Moreover, the interfacial charge transfer dynamics can be further controlled by EEF; namely, it not only modifies the band offset and the density of charge carrier donor and acceptor states, but also significantly modulates the strength of phonon excitation participating in *e-ph* coupling, which collectively determines the interfacial charge transfer dynamics. Particularly, positive EEF can sustain the ultrafast carrier dynamics and facilitate the separation of electron and hole. The present findings are expected to provide valuable insights on design and modulation of high-performance functional photovoltaic devices and photocatalysts.

[1] F. Xia, H. Wang, D. Xiao, M. Dubey, and A. Ramasubramaniam, Nat. Photon. **8**, 899 (2014).

[2] G. Fiori, F. Bonaccorso, G. Iannaccone, T. Palacios, D. Neumaier, A. Seabaugh, S. K. Banerjee, and L. Colombo, Nat. Nanotechnol. **9**, 768 (2014).

[3] M. Chhowalla, D. Jena, and H. Zhang, Nat. Rev. Mater. **1**, 16052 (2016).

[4] A. Avsar, H. Ochoa, F. Guinea, B. Özyilmaz, B. J. van Wees, and I. J. Vera-Marun, Rev. Mod. Phys. **92**, 021003 (2020).

[5] K. Iordanidou and J. Wiktor, Phys. Rev. Mater. **6**, 084001 (2022).

[6] I. I. Naumov and P. Dev, Phys. Rev. Res. **2**, 023157 (2020).

[7] K. S. Novoselov, A. Mishchenko, A. Carvalho, and A. H. Castro Neto, Science **353**, aac9439 (2016).

[8] Y. Liu, N. O. Weiss, X. Duan, H.-C. Cheng, Y. Huang, and X. Duan, Nat. Rev. Mater. **1**, 16042 (2016).

[9] H. Jin, H. Su, X. Li, Y. Yu, H. Guo, and Y. Wei, Phys. Rev. B **104**, 195404 (2021).

[10] X. Tan, L. Ding, G.-F. Du, and H.-H. Fu, Phys. Rev. B **103**, 115415 (2021).

[11] Z. Zhou, X. Zhang, Y. Guo, Y. Zhang, X. Niu, L. Ma, and J. Wang, Phys. Rev. B **103**, 245411 (2021).

[12] Q. Lv, F. Yan, N. Mori, W. Zhu, C. Hu, Z. R. Kudrynskyi, Z. D. Kovalyuk, A. Patanè, and K. Wang, Adv. Funct. Mater. **30**, 1910713 (2020).

[13] W. Ahmad, J. Liu, J. Jiang, Q. Hao, D. Wu, Y. Ke, H. Gan, V. Laxmi, Z. Ouyang, F. Ouyang *et al.*, Adv. Funct. Mater. **31**, 2104143 (2021).

[14] Q. Zheng, W. A. Saidi, Y. Xie, Z. Lan, O. V. Prezhdo, H. Petek, and J. Zhao, Nano Lett. **17**, 6435 (2017).

[15] X. Zhou, X. Hu, J. Yu, S. Liu, Z. Shu, Q. Zhang, H. Li, Y. Ma, H. Xu, and T. Zhai, Adv. Funct. Mater. **28**, 1706587 (2018).

[16] S. Zhao, B. Dong, H. Wang, H. Wang, Y. Zhang, Z. V. Han, and H. Zhang, Nanoscale Adv. **2**, 109 (2020).

[17] N. Youngblood, C. Chen, S. J. Koester, and M. Li, Nat. Photon. **9**, 247 (2015).

[18] M. Huang, M. Wang, C. Chen, Z. Ma, X. Li, J. Han, and Y. Wu, Adv. Mater. **28**, 3481 (2016).

[19] M. Talib, R. Tabassum, S. S. Islam Abid, and P. Mishra, ACS Omega **4**, 6180 (2019).

[20] S. Liu, W. Xiao, M. Zhong, L. Pan, X. Wang, H.-X. Deng, J. Liu, J. Li, and Z. Wei, Nanotechnology **29**, 184002 (2018).

[21] L. Li, Y. Yu, G. J. Ye, Q. Ge, X. Ou, H. Wu, D. Feng, X. H. Chen, and Y. Zhang, Nat. Nanotechnol. **9**, 372 (2014).

[22] F. Xia, H. Wang, and Y. Jia, Nat. Commun. **5**, 4458 (2014).

[23] J. Qiao, X. Kong, Z. X. Hu, F. Yang, and W. Ji, Nat. Commun. **5**, 4475 (2014).

[24] H. Liu, A. T. Neal, Z. Zhu, Z. Luo, X. Xu, D. Tomanek, and P. D. Ye, ACS Nano **8**, 4033 (2014).

[25] L. Li, J. Kim, C. Jin, G. J. Ye, D. Y. Qiu, F. H. da Jornada, Z. Shi, L. Chen, Z. Zhang, F. Yang *et al.*, Nat. Nanotechnol. **12**, 21 (2017).

[26] J. D. Wood, S. A. Wells, D. Jariwala, K. S. Chen, E. Cho, V. K. Sangwan, X. Liu, L. J. Lauhon, T. J. Marks, and M. C. Hersam, Nano Lett. **14**, 6964 (2014).

[27] R. A. Doganov, E. C. O'Farrell, S. P. Koenig, Y. Yeo, A. Ziletti, A. Carvalho, D. K. Campbell, D. F. Coker, K. Watanabe, T. Taniguchi *et al.*, Nat. Commun. **6**, 6647 (2015).

[28] J. Dai and X. C. Zeng, Angew. Chem. Int. Ed. **54**, 7572 (2015).

[29] J. O. Island, M. Barawi, R. Biele, A. Almazán, J. M. Clamagirand, J. R. Ares, C. Sánchez, H. S. J. van der Zant, J. V. Álvarez, R. D'Agosta *et al.*, Adv. Mater. **27**, 2595 (2015).

[30] N. Tripathi, V. Pavelyev, P. Sharma, S. Kumar, A. Rymzhina, and P. Mishra, Mater. Sci. Semicond. Process. **127**, 105699 (2021).

[31] S. Yang, M. Wu, W. Shen, L. Huang, S. Tongay, K. Wu, B. Wei, Y. Qin, Z. Wang, C. Jiang *et al.*, ACS Appl. Mater. Interfaces **11**, 3342 (2019).

[32] X. Wu, X. Chen, R. Yang, J. Zhan, Y. Ren, and K. Li, Small **18**, 2105877 (2022).

[33] Y. Liu, J. Zhang, S. Meng, C. Yam, and T. Frauenheim, Nano Lett. **21**, 4403 (2021).

[34] Y. Li, J.-K. Qin, C.-Y. Xu, J. Cao, Z.-Y. Sun, L.-P. Ma, P. A. Hu, W. Ren, and L. Zhen, Adv. Funct. Mater. **26**, 4319 (2016).

[35] F. Liu, J. Zhou, C. Zhu, and Z. Liu, Adv. Funct. Mater. **27**, 1602404 (2017).

[36] H. T. T. Nguyen, T. V. Vu, V. T. Pham, N. N. Hieu, H. V. Phuc, B. D. Hoi, N. T. T. Binh, M. Idrees, B. Amin, and C. V. Nguyen, RSC Adv. **10**, 2967 (2020).

[37] Y. Q. Ma, X. Zhao, T. X. Wang, W. Li, X. L. Wang, S. S. Chang, Y. Li, M. Y. Zhao, and X. Q. Dai, Phys. Chem. Chem. Phys. **18**, 28466 (2016).

[38] L. Huang, N. J. Huo, Y. Li, H. Chen, J. H. Yang, Z. M. Wei, J. B. Li, and S. S. Li, J. Phys. Chem. Lett. **6**, 2483 (2015).

[39] W. Q. Xiong, C. X. Xia, X. Zhao, T. X. Wang, and Y. Jia, Carbon **109**, 737 (2016).

[40] X. Wang, R. Quhe, W. Cui, Y. Zhi, Y. Huang, Y. An, X. Dai, Y. Tang, W. Chen, Z. Wu *et al.*, Carbon **129**, 738 (2018).

[41] G. Cheng, M. M. Rahman, Z. He, A. L. Allcca, A. Rustagi, K. A. Stampe, Y. Zhu, S. Yan, S. Tian, Z. Mao *et al.*, Nat. Commun. **13**, 7348 (2022).

[42] A. V. Akimov, J. Phys. Chem. Lett. **9**, 6096 (2018).

[43] Q. Zheng, W. Chu, C. Zhao, L. Zhang, H. Guo, Y. Wang, X. Jiang, and J. Zhao, WIREs Comput. Mol. Sci. **9**, e1411 (2019).

[44] A. V. Akimov and O. V. Prezhdo, J. Chem. Theor. Comput. **9**, 4959 (2013).

[45] A. V. Akimov and O. V. Prezhdo, J. Chem. Theor. Comput. **10**, 789 (2014).

[46] L. Zhang, Q. Zheng, Y. Xie, Z. Lan, O. V. Prezhdo, W. A. Saidi, and J. Zhao, Nano Lett. **18**, 1592 (2018).

[47] W. Chu, Q. Zheng, O. V. Prezhdo, and J. Zhao, J. Am. Chem. Soc. **142**, 3214 (2020).

[48] W. Chu, W. A. Saidi, Q. Zheng, Y. Xie, Z. Lan, O. V. Prezhdo, H. Petek, and J. Zhao, J. Am. Chem. Soc. **138**, 13740 (2016).

[49] Y. Tian, Q. Zheng, and J. Zhao, J. Phys. Chem. Lett. **11**, 586 (2020).

[50] Y. Wang, Y. Shi, C. Zhao, Q. Zheng, and J. Zhao, Phys. Rev. B **99**, 165309 (2019).

[51] P. E. Blöchl, Phys. Rev. B **50**, 17953 (1994).

[52] J. P. Perdew, K. Burke, and M. Ernzerhof, Phys. Rev. Lett. **77**, 3865 (1996).

[53] S. Grimme, J. Comput. Chem. **27**, 1787 (2006).

[54] See Supplemental Material at http://link.aps.org/supplemental/10.1103/PhysRevB.109.075306 for the NAMD methodology; text of CONTCAR file; differential charge density distribution and photoabsorption spectra; charge density distribution under EEF; charge wave functions of electron donor state at representative snapshots; frozen phonon NAMD results for other representative phonon modes for charge transfer dynamics. It also contains Refs. [55–58].

[55] E. Runge and E. K. U. Gross, Phys. Rev. Lett. **52**, 997 (1984).

[56] S. Hammes-Schiffer and J. C. Tully, J. Chem. Phys. **101**, 4657 (1994).

[57] S. R. Billeter and A. Curioni, J. Chem. Phys. **122**, 034105 (2004).

[58] J. C. Tully, J. Chem. Phys. **93**, 1061 (1990).

[59] X. Zhao, M. Bo, Z. Huang, J. Zhou, C. Peng, and L. Li, Appl. Surf. Sci. **462**, 508 (2018).

[60] E. Mostaani, N. D. Drummond, and V. I. Fal'ko, Phys. Rev. Lett. **115**, 115501 (2015).

[61] T. Cao, X. Li, L. Liu, and J. Zhao, Comput. Mater. Sci. **112**, 297 (2016).

[62] V. R. Policht, M. Russo, F. Liu, C. Trovatello, M. Maiuri, Y. Bai, X. Zhu, S. Dal Conte, and G. Cerullo, Nano Lett. **21**, 4738 (2021).

[63] H. Zhu, J. Wang, Z. Gong, Y. D. Kim, J. Hone, and X. Y. Zhu, Nano Lett. **17**, 3591 (2017).

[64] X. Hong, J. Kim, S.-F. Shi, Y. Zhang, C. Jin, Y. Sun, S. Tongay, J. Wu, Y. Zhang, and F. Wang, Nat. Nanotechnol. **9**, 682 (2014).

[65] E. R. Bittner and C. Silva, Nat. Commun. **5**, 3119 (2014).

[66] Z. Zhou, Z. Zheng, J. He, J. Wang, O. V. Prezhdo, and T. Frauenheim, Nano Lett. **23**, 5688 (2023).

[67] J. He, S. Li, A. Bandyopadhyay, and T. Frauenheim, Nano Lett. **21**, 3237 (2021).